Structure, Volume *27*

Supplemental Information

Multisystem Proteinopathy Mutations in VCP/p97 Increase NPLOC4·UFD1L Binding and Substrate Processing

Emily E. Blythe, Stephanie N. Gates, Raymond J. Deshaies, and Andreas Martin

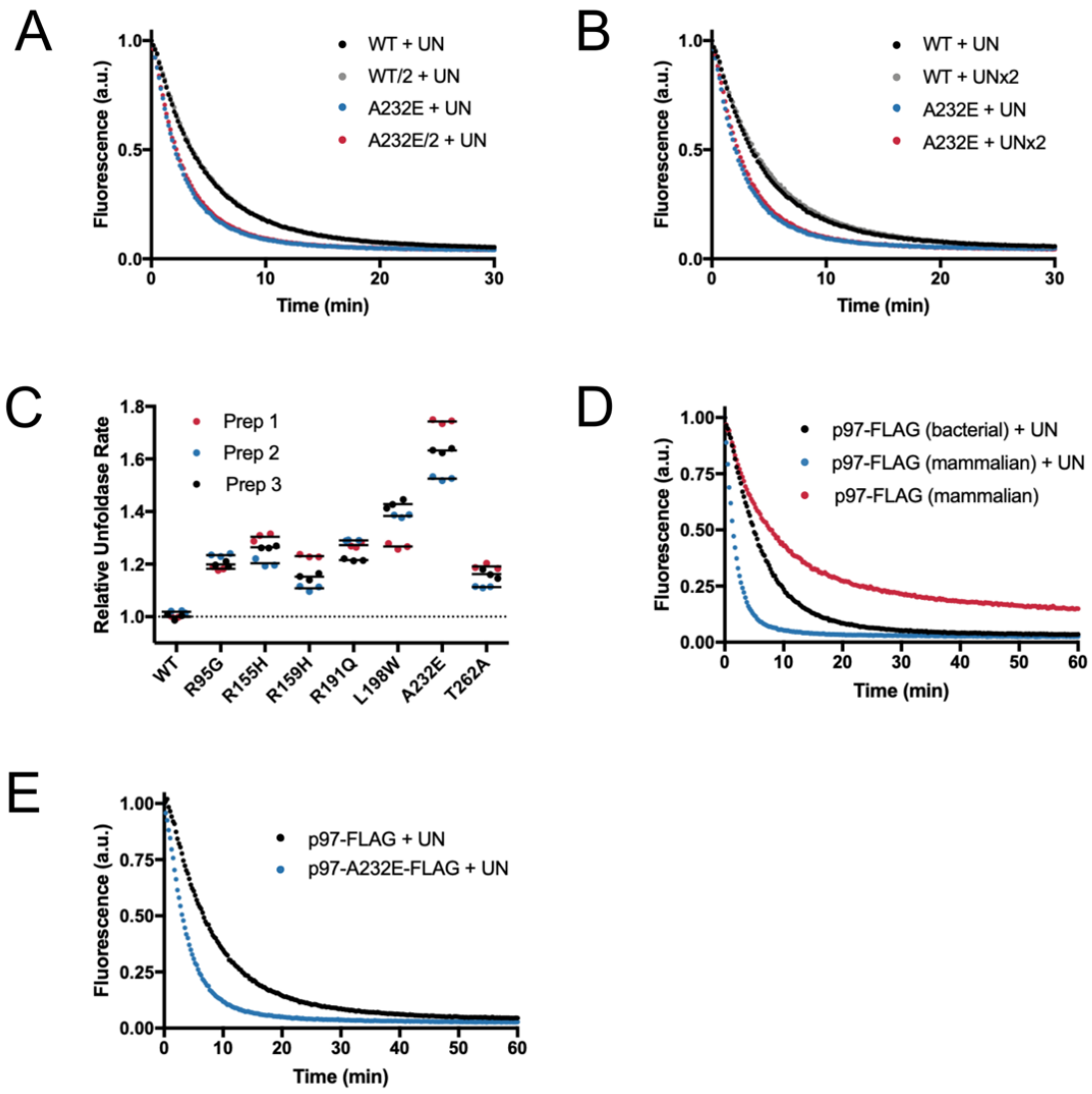

Figure S1. Related to Figure 1. (A) Example time courses of unfolding of split mEos3.2 show little change in normalized rate when the concentration of p97 is halved (WT: 0.985 ± 0.005, p97-A232E: 0.937 ± 0.006). **(B)** Example time courses show little change in normalized rate when UN is doubled (WT: 0.927 ± 0.002, p97-A232E: 0.93 ± 0.01). **(C)** Prep-to-prep variability in the unfoldase rates of MSP-mutant p97. All MSP mutants showed increased unfoldase rates compared to wild type yet with considerable prep-to-prep variabilities. For Preps 1 and 2, assays were carried out in a modified assay buffer under slightly different conditions (see Methods), and substrate-unfoldase rates were normalized to that of wild-type p97 Prep 1. The rates for the Prep 3 are replotted from Figure 1C. **(D)** Example mEos3.2 substrate-unfolding traces show that human cell-line expressed p97 in complex with UN (blue trace) is a faster unfoldase than *E. coli*-expressed p97·UN (black trace) and can promote unfolding even without the addition of exogenous UN (red trace). **(E)** Example unfolding traces show human cell-line expressed p97-A232E unfolds substrate faster than similarly expressed wild-type p97. Representative traces shown. Technical replicates, n ≥ 2, ± S.D..

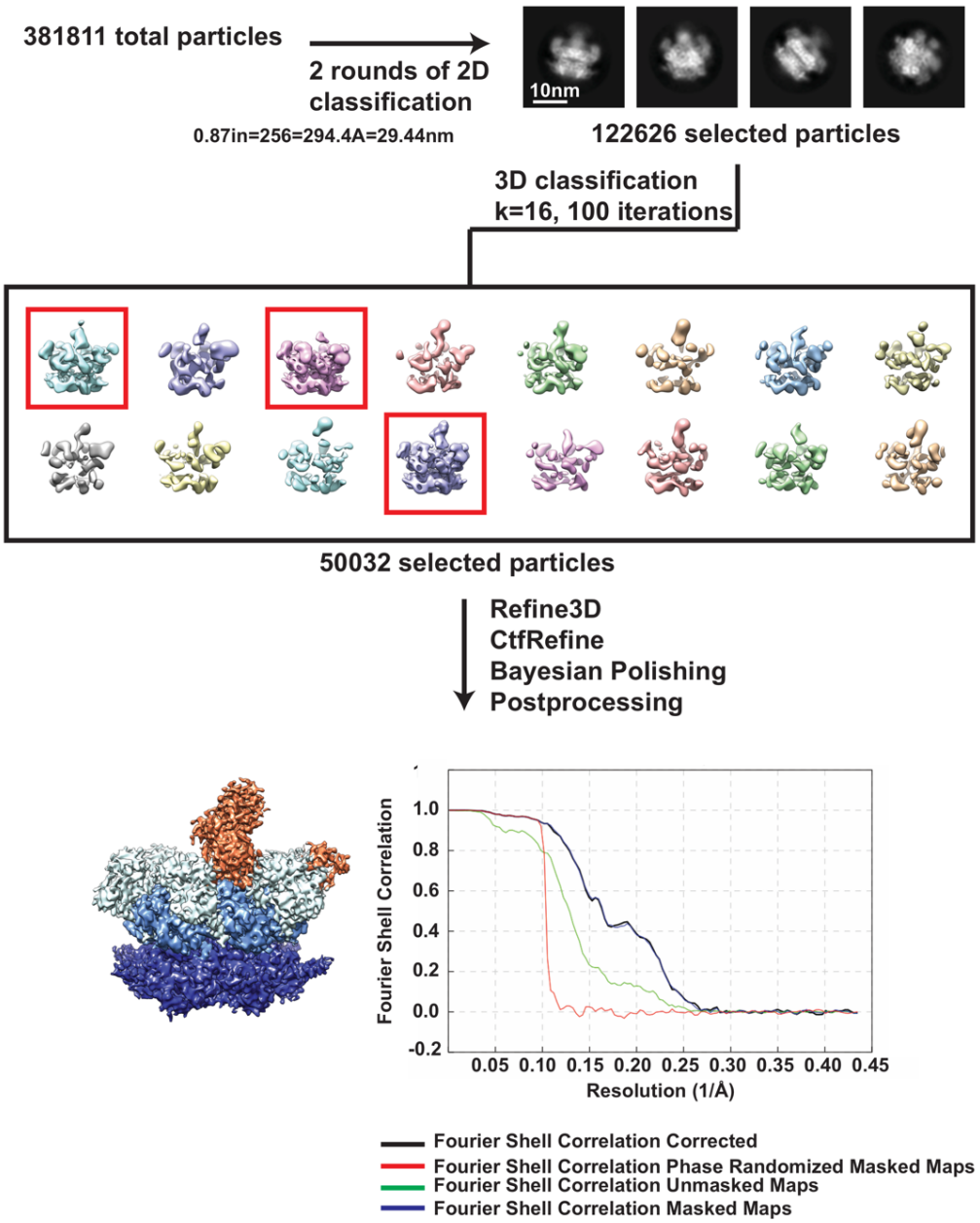

Figure S2. Related to Figure 3. Analysis and cryo-EM processing of the p97-A232E:UN-ATP complex. Total particles of p97-A232E:UN-ATP complex dataset were subjected to two rounds of reference-free 2D class averages to clean out contamination or bad particles, followed by a 3D classification into 16 classes. The three best classes of particles were selected from the total 16 classes (red box), resulting in a final dataset of 50,032 particles. This particle stack was refined with CtfRefinement, Bayesian polishing, and post-processing, resulting in a final resolution of 4.26Å, evaluated using gold standard FSC curves of the masked and unmasked post-processed final reconstructions (Scheres, 2012). The final map is colored by domains: NPLOC4 (orange), NTDs (light blue), D1 (sky blue), D2 (navy blue).

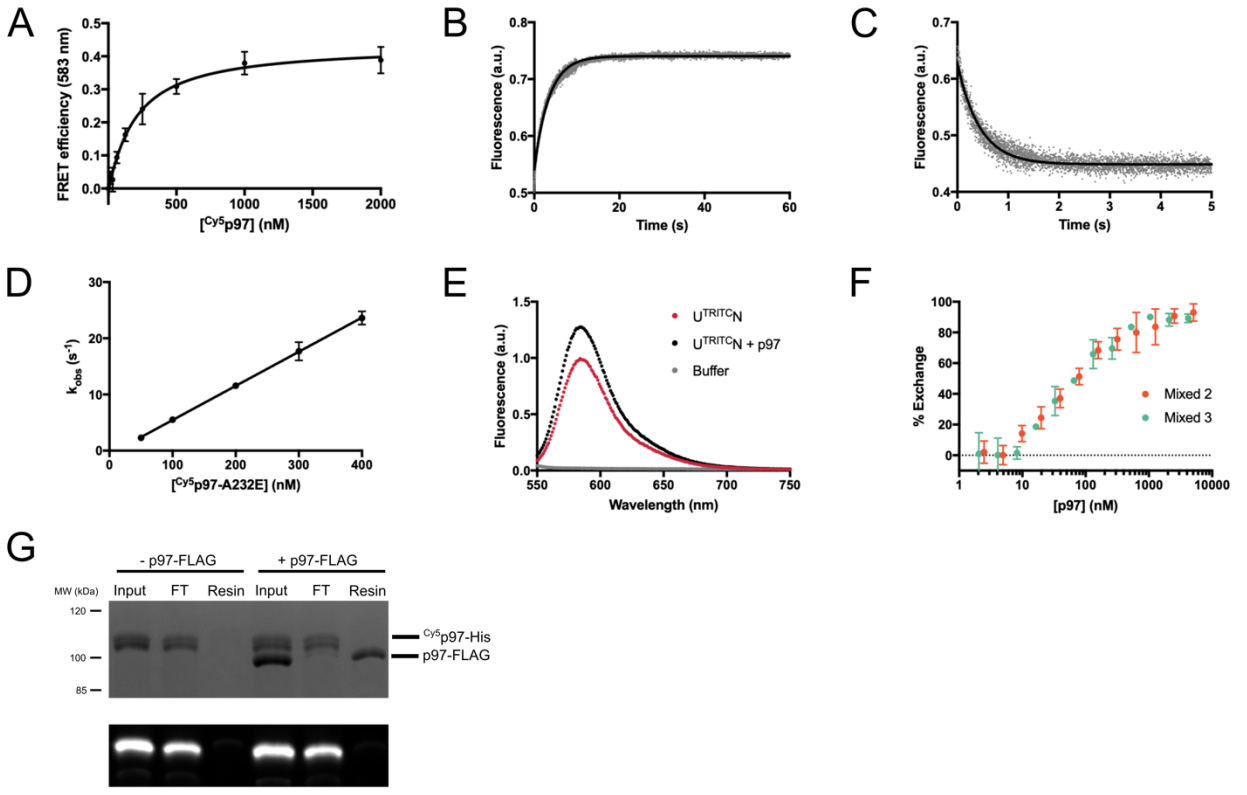

Figure S3. Related to Figure 5 and Table 1. (A) Example FRET-based binding curve for the interaction of $U^{TRITC}N$ with variable concentrations of $^{Cy5}p97$ in ATPγS. Data were fit to a quadratic binding equation (technical replicates, N = 3, ± S.D.). **(B)** Example trace and single-exponential fit for the dissociation of $U^{TRITC}N$ from $^{Cy5}p97$ in ATPγS, measured by the recovery of donor TRITC fluorescence after stopped-flow mixing. **(C)** Example trace and single-exponential fit for the binding of $U^{TRITC}N$ to $^{Cy5}p97$ in ATPγS, measured by the quenching of donor TRITC fluorescence after stopped-flow mixing. **(D)** Shown are the observed rate constants k_{obs} for the association of $U^{TRITC}N$ with $^{Cy5}p97$-A232E in ATPγS, derived from single-exponential fits of binding kinetics at various $^{Cy5}p97$-A232E concentrations. The association rate constant, k_{on}, was determined by linear regression (technical replicates, N ≥ 5, ± S.D.). **(E)** $U^{TRITC}N$ fluorescence (red, 50 nM) is sensitive to binding of unlabeled p97 (black, 2.5 μM). (**F**) Competition FRET experiment, monitoring the dissociation of $U^{TRITC}N$ from Cy5-labeled p97-A232E and binding to excess unlabeled Mixed 2 and Mixed 3 heterohexamers, show that the mixed heterohexamers have similar UN affinities (technical replicates, N ≥ 2, ± S.D.). **(G)** Protomer exchange between p97 hexamers is slow. Coomassie stain and fluorescence scan of an SDS-PAGE gel show no evidence of His-tagged $^{Cy5}p97$ binding to the anti-FLAG resin despite robust binding of FLAG-tagged p97.

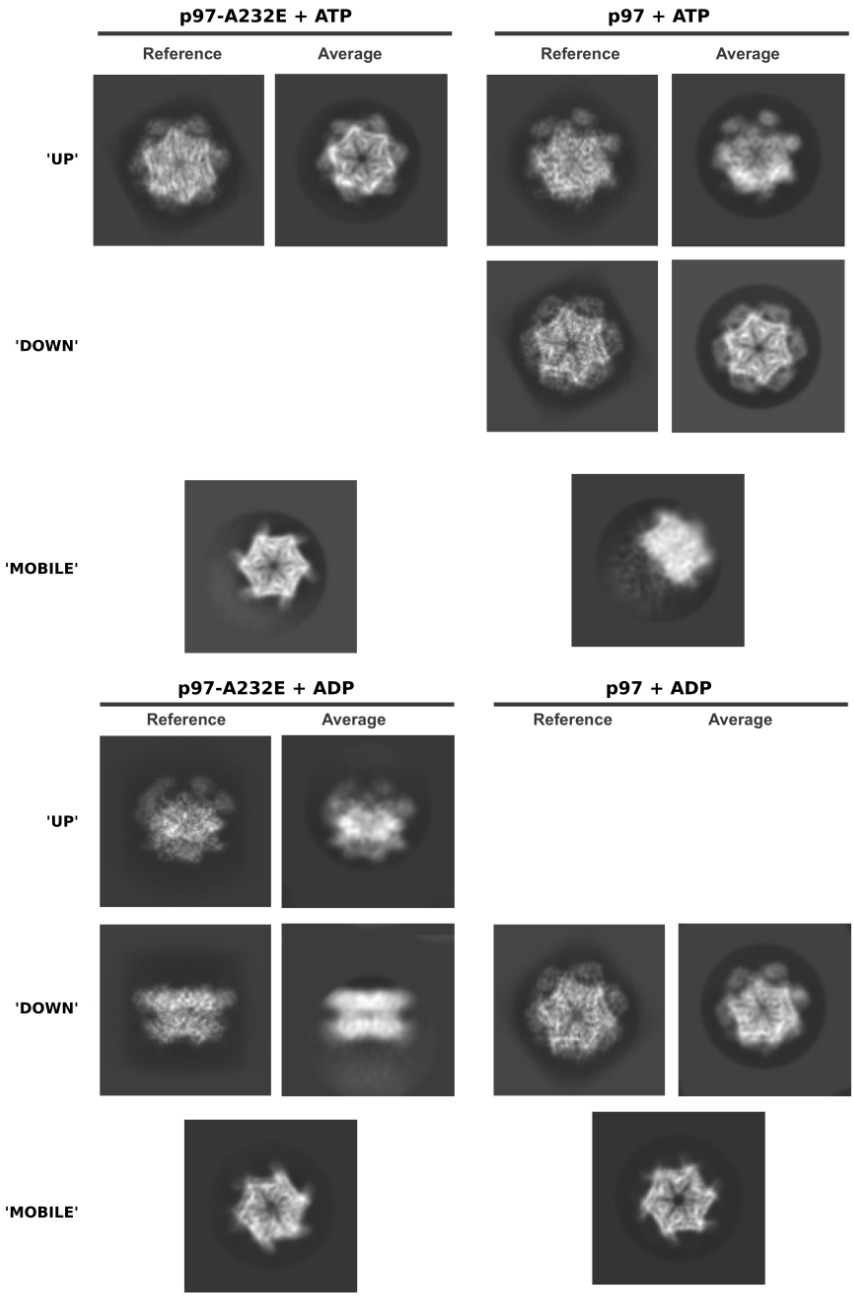

Figure S4: Related to Figure 6. Representative 2D class averages of nucleotide datasets, compared to back projections of 3D models. Back projections of the 3D models for p97-ATPγS (EMD:3297) and p97-ADP (EMD:3299) (Banerjee et al., 2016) next to a representative 2D class average from each nucleotide dataset, oriented in the same angle. Representative averages are also shown for hexamers with ‘mobile’ NTDs.

	p97-A232E-UN:ATP	p97-ATP	p97-A232E-ATP	p97-ADP	p97-A232E-ADP
Microscope	Titan Krios	Talos Arctica			
Nominal Mag.	33,333x	43,860x			
Detector	K2			K3	
Pixel Size (Å/pixel)	1.15	1.16		1.14	
Exposure (s)	8			5.273	
Frame rate (s)	0.2			0.12	
Total electron dose	48				
Defocus Range (μm)	-1 to -2.5				
Total Micrographs	5897	1100	704	706	1781
Total Particles	164673	170204	141281	414495	181424

Table S1. Related to Figure 3 and Figure 6. Parameters for the cryo-EM data collection.